Revised manuscript (clean version) Click here to view linked References

Deciphering membrane biofouling induced by micro-/nano-plastics in nanofiltration: Metagenomic insights and spacer-driven mitigations

Xinhui Liu[a], Yu Yang[a, *], Nigel J D Graham[b], Satoshi Takizawa[c], How Yong Ng[d,e]

[a] School of Environment, Beijing Normal University, Beijing, 100875, China

[b] Department of Civil and Environmental Engineering, Imperial College London, South Kensington Campus, London SW7 2AZ, United Kingdom

[c] Department of Urban Engineering, Graduate School of Engineering, The University of Tokyo, 7-3-1 Hongo, Bunkyo-ku, Tokyo 113-8656, Japan

[d] Center for Water Research, Advanced Institute of Natural Sciences, Beijing Normal University, Zhuhai 519087, China

[e] National University of Singapore Environmental Research Institute, 5A Engineering Drive 1, Singapore 117411, Singapore

[*] **CORRESPONDING AUTHOR**

Yu Yang E-mail address: yangyu@bnu.edu.cn

Abstract

Nanofiltration (NF) is an effective process for micro-/nano-plastics (MNPs) interception, but the impact of accumulated MNPs on the microbial community structure and metabolic pathways of biofilms on NF membranes remains unclear. This provides uncertainty with respect to membrane biofouling behavior and the risks to efficient NF operations. In this study, the size-dependent (20 nm–25 μm) and concentration-dependent (0.1–50 $mg \cdot L^{-1}$) effects of MNPs on the biofouling of a NF membrane treating secondary wastewater effluent were studied. Three MNPs-tolerant, hypermetabolic and polystyrene-degradable genera (i.e., *Acinetobacter*, *Novosphingobium* and *Asticcacaulis*) were detected in biofilms as dominant taxonomic compositions. MNPs led to an increase of 19.3%–76.7% in biomass contents and a more rapid decrease in permeate flux, with 0.1 $mg \cdot L^{-1}$ of 80 nm NPs causing the most severe membrane biofouling. Metagenomic analysis revealed that MNPs upregulated enzymes involved in exopolysaccharide (ExoA/L/M/P/Q/X/Y/Z) and tyrosine (COMT, FeaB and AOC3) biosynthesis and quorum sensing (PhzF and CiaH/R), and suppressed cell motility pathways including flagellar assembly and bacterial chemotaxis. Novel types of perforated column spacer (PCS) enhanced the hydrodynamics of the membrane feed with a lower pressure drop and higher fluid velocity, introduced micro-jets and greater mass transfer inside feed channels, thus eliminating the deposition of MNPs and mitigating membrane biofouling. Overall, a greater understanding of the interaction mechanisms between MNPs and membrane biofouling in secondary effluent filtration will help develop more effective MNPs

management strategies and achieve more sustainable NF operations.

Keywords: Nanofiltration (NF); Micro-/nano-plastics (MNPs); Membrane biofouling; Effluent treatment; Spacer modification; Computational fluid dynamics (CFD)

1. Introduction

The presence of micro-plastics (MPs) and nano-plastics (NPs) in wastewater treatment plants (WWTPs) has attracted extensive attention because of their ubiquitous occurrence and persistent ecological hazards (Dronjak et al., 2022; Mintenig et al., 2017; Sarkar et al., 2021). Nanofiltration (NF) has the advantages of producing an excellent permeate quality and high resource recovery, which make it suitable as a tertiary treatment process and it has shown promise in mitigating the efflux of micro-/nano-plastics (MNPs) (Wang et al., 2020; Ye et al., 2019). However, the MNPs particles deposition on the NF membrane surface tend to increase water transfer resistance (reduced permeability) and pose potential membrane fouling issues (Toh et al., 2020; 2022). Polystyrene NPs have been reported to promote heterogeneous nucleation of silica and humic acid (HA) adsorption, and induce the formation of stable composite pollutants on the membrane surface (Yang et al., 2024). To date, little is known about the effect of MNPs on the development of membrane biofouling, which remains the primary challenge in full-scale NF applications because of the associated increase in operational costs.

MNPs can have a significant impact on microbial taxonomical structure and biosynthetic metabolism (Kang et al., 2022; Yang et al., 2020). It has been found that

MNPs diminished the abundance of denitrifiers in activated sludge, suppressed the expression of functional genes involved in nitrogen transformations and reduced denitrification efficiency (Huang et al., 2023). In another study, MNPs enriched the potential hosts of antibiotic resistance genes (ARGs) *Thauera* and *Dokdonella*, and increased the propagation of ARGs in sequencing batch reactors (Zhou et al., 2022). In addition, MPs reshaped the fate of aqueous carbon by enriching heterotrophic microbes and stimulating the tricarboxylic acid (TCA) cycle to accelerate the bio-degradation process of dissolved organic matter (DOM) (Liu et al., 2023b). Therefore, as MNPs are rejected by NF and interact with the membrane surface bacteria, they might have positive or negative effects on the membrane biofouling behavior by altering the composition and functions of the microbial community. Considering the potential interactions of MNPs–MNPs, MNPs–bacteria and MNPs–membrane surface, during nanofiltration, it is necessary to investigate the occurrence and mechanisms of MNPs effects on membrane biofouling as NF is being to be widely adopted for water reuse.

Biofilm attachment and growth on membrane surface are significantly influenced by localized hydrodynamics within the feed channel, where inducing turbulence is essential to alleviate membrane biofouling and support long-term NF operations (Kerdi et al., 2021). Periodic cleaning and modifications to the spacer geometry (e.g., internal strand angle, strand thickness, spacer filament shape and porosity) are effective methods to improve hydraulic conditions and inhibit foulant accumulation (Giagnorio et al., 2019; Lin et al., 2021). Intrinsically modifying cylindrical filaments through

perforation has been reported to improve permeate production by introducing micro-jets and generating strong shear stress fluctuations inside the filament cell (Kerdi et al., 2018). In another study, the column nodes function as additional vortex shaking bodies, contributing to the enhancement of unsteady conditions around nodes and inducing the emanations of feed flow in the spacer filled channel (Ali et al., 2019). Therefore, a more advanced geometry of the perforated column spacer is expected to achieve the synergistic effect of micro-jets and vortex shaking bodies, which has the potential to eliminate MNPs deposition and enhance the permeability of nanofiltration. Computational fluid dynamics (CFD) simulations reveal the critical relationship between feed spacer characteristics and three key phenomena: flow field distribution, MNPs transportation and deposition behavior, as well as biofilm attachment and growth mechanisms (Ali et al., 2019; Lin et al., 2020). The integrated approach of CFD-guided spacer design demonstrates potential to produce flow perturbation, reduce MNPs deposition and enhance NF performance.

To understand the effects of MNPs on NF membrane biofouling, this study investigated the variation of microbial community structure and biosynthetic metabolism with size-dependent (20 nm–25 μm) and concentration-dependent (0.1–50 $mg \cdot L^{-1}$) MNPs suspended in real secondary effluent. Characterization of extracellular polymeric substances (EPS) and cyclic physical cleaning were conducted at different operation times to evaluate the biofouling variations with MNPs stress. Microbial metabolic pathways and functional gene expressions were explored by 16S rRNA gene sequencing and metagenome analysis. Computational fluid dynamic (CFD) modeling

were performed to optimize the spacer design, clarify local hydrodynamics and simulate MNPs deposition positions, combined with the discrete phase model (DPM). Overall, for the first time, this work has revealed the underlying mechanisms of microbial diversity and bio-functional interactions in nanofiltration under MNPs exposure, which will help to develop effective MNPs management strategies in the use of the NF process and potentially other water treatment processes.

2. Materials and methods

2.1 Micro/nanoplastics and secondary effluents

Non-additive polystyrene MNPs with diameters of 20 nm, 80 nm, 1 μm and 25 μm were chosen as the model MNPs in this study and were purchased from Beisile Co., Ltd. (Tianjin, China). Unless otherwise specified, all MNPs used in this study are made of polystyrene. Prior to usage, the stock solutions were sonicated for 30 min to promote the uniform distribution of MNPs particles. We tested MNPs concentrations spanning 0.1–50 $mg \cdot L^{-1}$, a range that reflects environmental scenarios, follows standard toxicological testing concentrations, and aligns with previous studies (Enfrin et al., 2021; Kang et al., 2022; LaRue et al., 2022). The secondary effluents were collected from the Gaobeidian Wastewater Treatment Plant in Beijing, China. All water samples were pre-filtered through a 0.45-μm cellulose ester membranes (Tengjin, China) to remove suspended particles and then stored at 4°C. To ensure sample stability and minimize potential changes in microbial composition or chemical properties, the treated water samples were used for experiments within two weeks. The ion

concentrations of the raw secondary effluent were provided in the Supporting Information (SI, Table S1). A commercial polyamide thin-film composite flat sheet NF270 membrane was used in the tests and provided by DuPont (FilmTec™, USA). Detailed basic NF270 membrane properties were shown in Table S2.

2.2 NF system setup and filtration experiments

Nanofiltration system setup and dynamic filtration experiments were carried out according to previous research studies (Cui et al., 2015; Wang et al., 2020). The commercial NF270 membrane was preconditioned by storing it in a 1.5% (w/v) $NaHSO_3$ solution. Before filtration experiments, the flat sheet NF270 membrane was rinsed with copious amounts of deionized (DI) water to remove any residual preservative and then soaked for at least 24 h. This step ensured the membrane remained moist, facilitated flux recovery, and inhibited bacterial growth. A cross-flow apparatus with an effective filtration area of 19.25 cm^2 (3.5 cm × 5.5 cm) was constructed for membrane biofouling studies, and a schematic depiction of the experimental set-up is shown in Fig. S1. Before initiating the biofouling process, the entire system was thoroughly disinfected overnight using anhydrous ethanol of analytical grade, followed by rinsing with sterile deionized water to ensure cleanliness (Song et al., 2023). To eliminate compaction during the filtration, the membrane coupons were compacted at 0.8 MPa for 3 h feed with deionized water. After achieving a stable flow, secondary effluents, with the addition of 80 nm NPs (0.1–50 $mg \cdot L^{-1}$) or 0.1 $mg \cdot L^{-1}$ MNPs (20 nm–25 μm), were applied to the NF system at a surface pressure of 0.6 MPa for 36 h and 30 day, respectively (Table 1). The mass of permeate water

collected from the filter cell was recorded gravimetrically and logged by computer every 10 min using RsMulti software (A&D, Company), and the membrane concentrate solution was recirculated to the feed tank.

Table 1. The feed composition and filtration period of nanofiltration systems.

Label	Filtration period	MNPs size	MNPs dosing concentration
S0	36 h	/	0 $mg \cdot L^{-1}$
SC0.1	36 h	80 nm	0.1 $mg \cdot L^{-1}$
SC1	36 h	80 nm	1 $mg \cdot L^{-1}$
SC10	36 h	80 nm	10 $mg \cdot L^{-1}$
SC50	36 h	80 nm	50 $mg \cdot L^{-1}$
L0	30 day	/	0 $mg \cdot L^{-1}$
LN20	30 day	20 nm	0.1 $mg \cdot L^{-1}$
LN80	30 day	80 nm	0.1 $mg \cdot L^{-1}$
LM1	30 day	1 μm	0.1 $mg \cdot L^{-1}$
LM25	30 day	25 μm	0.1 $mg \cdot L^{-1}$

The permeate flux (J, $L \cdot m^{-2} \cdot h^{-1}$, LMH) was calculated according to Eq. (1):

$$J = \frac{W}{A \times t} \quad (1)$$

where, W is the permeation volume (L), A represents the effective area of membrane (m^2) and t means the filtration time (h). Normalized flux (J/J_0) was used to represent the membrane permeate performance as a function of time, according to Eq. (2):

$$\text{Normalized flux} = \frac{J}{J_0} \quad (2)$$

where J (LMH) is the measured permeate flux at a specific time and J_0 (LMH) represents the initial membrane flux. All filtration experiments were conducted in triplicate.

2.3 Physicochemical analysis of membrane biofouling

At the end of filtration experiments, fouled membranes were carefully removed from the membrane tanks and EPS isolation was conducted for biofilm composition analysis as described in the literature (Du et al., 2021; Siddiqui et al., 2017; Xiong et al., 2022). The phenol-sulfuric acid method and Bradford protein assay kit (Beyotime, China) were used to determine the polysaccharide and protein contents, respectively (Dubois et al., 1956). All measurements were performed in triplicate for each parameter, and the results were expressed as mean values ± standard deviation (SD). The significance of differences among groups were analyzed by one-way analysis of variance (ANOVA) with an acceptance significance of $p < 0.05$.

2.4 Physical cleaning strategy and fouling resistance of membrane

Revealing the biofouling mechanisms of NF membrane by MNPs to develop appropriate cleaning procedures is crucial for removing deposited MNPs particles and foulants from the membrane surface, as well as ensuring sustainable filtration operation. To evaluate the performance of optimized spacers in enhancing flux recovery and mitigating fouling, we conduct cyclic physical cleaning in repeated short-term experiments (36 h, 80 nm, 0.1–50 $mg \cdot L^{-1}$). Different with the continuous dynamic filtration experiments, the system was washed with deionized water for 30 min after 6 h, 12 h, 24 h and 36 h of biofouling, under zero transmembrane pressure conditions (Zhang et al., 2025). The flux recovery ratio (FRR, %), physically irreversible fouling ratio (FR_{ir}, %), and physically reversible fouling ratio (FR_r, %) were calculated according to Eqs. (3–5) (Song et al., 2023; Wang et al., 2018).

$$\mathrm{FRR} = \frac{J_c}{J_0} \times 100\% \quad (3)$$

$$\mathrm{FR_{ir}} = \left(1 - \frac{J_c}{J_0}\right) \times 100\% \quad (4)$$

$$\mathrm{FR_r} = \left(\frac{J_c - J_f}{J_0}\right) \times 100\% \quad (5)$$

where J_0 (LMH) represents the initial membrane flux, J_f (LMH) is the permeate flux after periodic contamination, J_c (LMH) is the permeate flux after 0.5 h hydrodynamic cleaning using DI water.

2.5 DNA extraction, 16S rRNA gene sequencing and metagenomics analysis

The collected membrane biofilm samples after 36 h and 30 day filtration were analyzed to identify microbial community structures. The Fast DNA® SPIN Kits (MP Biomedicals, Santa Ana, USA) were employed for genomic DNA extraction according to the manufacturer's instruction. Primers 338F (5'-ACTCCTACGGGAGGCAGCAG-3') and 806R (5'-GGACTACHVGGGTWTCTAAT-3') were used to amplify the V3–V4 hyper variable regions of bacterial 16S rRNA genes. Polymerase chain reaction (PCR) analysis was conducted with the following cycle profile: denature at 95°C for 3 min, followed by 25 cycles of 95°C for 30 s, annealing at 57°C for 30 s, 72°C for 45 s, and lastly with an extension at 72°C for 10 min. The purified product was detected by use of an Illumina MiSeq sequencer in Sangon Biotech Co., Ltd. (Shanghai, China). The sequence reads were clustered into operational taxonomic units (OTUs) at a similarity threshold of 97% on the i-Sanger platform, and the total sequencing reads were

annotated against the Kyoto Encyclopedia of Genes and Genomes (KEGG) databases (Xu et al., 2023).

DNA samples collected from 30 day filtration experiments were selected to perform metagenomics sequencing on the Illumina HiSeq 2500 platform (Majorbio Biotechnology, Shanghai). Megahit (https://github.com/voutcn/megahit) was used to stitch the reads together into contigs. MetaGene (http://metagene.cb.k.u-tokyo.ac.jp/) was used to predict the open reading frames (ORFs) of contigs, and the ORFs with a length ≥100 bp were further selected and translated to amino acid sequences (Huang et al., 2023). Then, CD-HIT (http://www.bioinformatics.org/cd-hit/) was used to cluster all the predicted genes with a 90% sequence identity and 0.9 coverage (Wang et al., 2022). SOAPaligner (http://soap.genomics.org.cn/) was used to align the high-quality reads to the non-redundant gene catalogs with 95% identity (Li et al., 2022). Taxonomic and functional annotations were conducted using BLASTp by comparing the non-redundant gene catalogs with the NCBI NR database (e-value ≤ $1e^{-5}$), as well as the KEGG database (https://ftp.ncbi.nlm.nih.gov/blast/db/FASTA/). Gene set enrichment analysis (GSEA), determined whether an *a priori* defined set of genes in specific pathway, showed statistically significant and concordant differences between two biological states (https://www.gsea-msigdb.org/gsea/index.jsp).

2.6 Co-occurrence network analyses

Microbial co-occurrence network analysis was conducted to illustrate the correlations among multi-species. Specifically, the relative abundance of OTU was firstly converted into binary data, with a value of 1 representing the presence of OTU,

223 and a value 0 representing absence. After that, the datasets were imported into R, in
224 which only the robust correlations (p value < 0.01, coefficient (rho) > |0.6|) were
225 included to determine the co-occurrence networks (Xu and He, 2022). R packages
226 igraph, hmisc, ggplot2, ggpubr and ggsignif, were used to perform all network analyses.
227 The normalized classification data along with the output from the co-occurrence
228 analysis were visualized by Gephi interactive platform (http://gephi.guthub.io/) for the
229 network diagram creation and calculation of network topological indices.

230 **2.7 Feed spacer designs and 3D printing**

231 The modeling of feed spacers was designed by Computer Aided Design software
232 (AutoCAD, Version 2021), and the standard spacer and perforated column spacers
233 (with hole diameters of 0.5 and 0.3 mm) were denoted as SS, PCS_0.5 and PCS_0.3,
234 respectively. The strand angle (α) and the incident flow angle (β) were set to be 45° and
235 90°, respectively, as previous research had suggested (Kerdi et al., 2018). Fig. 1 shows
236 the schematic and typical dimensions of the spacer configuration. A high-resolution of
237 3D-printing technology (2-μm printing layer) was adopted in the rapid prototyping of
238 feed spacers (Fig. S2). Spacers were printed in a rectangular frame (3.5 cm × 5.5 cm ×
239 1.2 mm) to fit the flow cell size, using the photopolymer (HTL resin, Table S3).

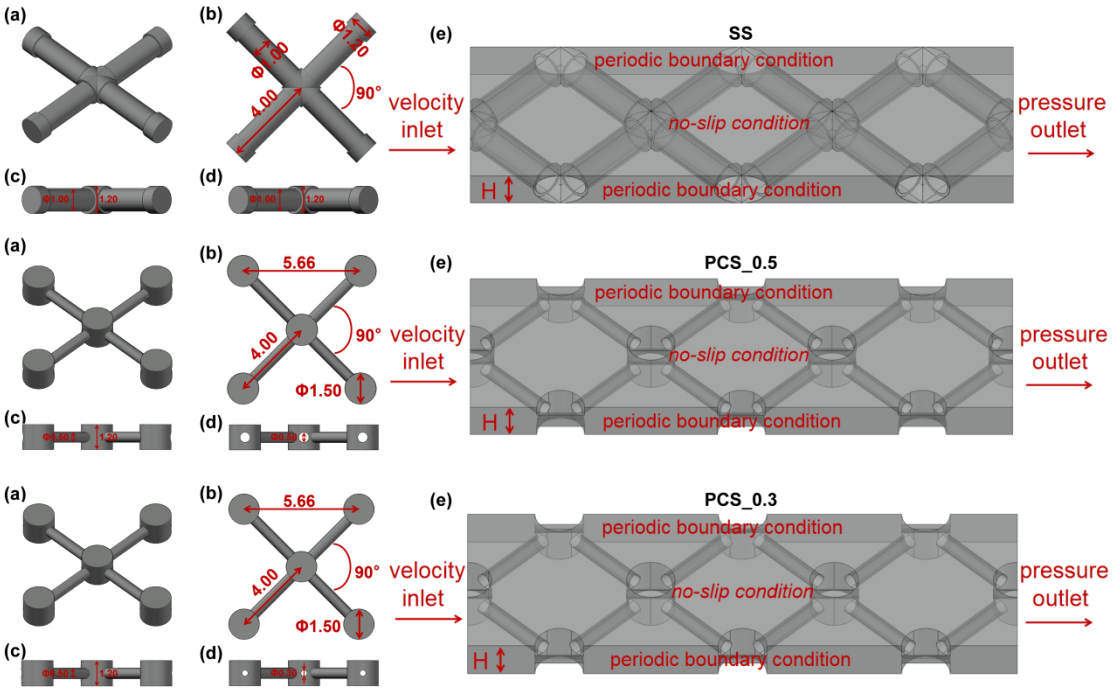


Fig. 1. Schematic of feed spacers with all dimensions in mm: The monomer model (a), top view (b), front view (c), left view, (d) and fluid domain models (i.e., the difference between the rectangular block and the spacer geometry) with the description of boundary conditions (e). The membrane walls were considered impermeable, and periodic boundary conditions were imposed at lateral boundaries to eliminate the wall effect.

2.8 Numerical approach and CFD-DPM simulation

The hydrodynamic behavior in the presence of three feed spacers were studied computationally. Specifically, the temporal and spatial distribution of velocity, pressure and streamlines across the filtration feed channels were explored by the direct numerical simulation (DNS) approach. The feed was considered as a Newtonian fluid, and the Continuity equation and Navier-Stokes equation used were given by a previous study (Ali et al., 2019):

$$\nabla \cdot u = 0 \tag{6}$$

$$\rho(\frac{\delta u}{\delta t} + (u \cdot \nabla)u) = \rho g - \nabla p + \mu \nabla^2 u \tag{7}$$

where t and u stand for the time and the velocity vector, respectively; p represents the pressure and ∇ means the spatial gradient; ρ and g are the fluid density and the gravitational acceleration, respectively.

The discrete phase model (DPM) is directly concerned with defining particle behavior inside a continuum fluid, suitable for fluids having low solid densities (i.e., less than 10%) (Karakurt et al., 2018). In this study, the CFD-DPM model was used to track MNPs particles inside feed channels, and the particle–particle and particle–wall interactions were ignored (Huang et al., 2021). The MNPs particles were tracked based on integrating the following equations (Morsi and Alexander, 1972; Ounis et al., 1991; Shukla et al., 2011):

$$\frac{du_p}{dt} = \frac{18\mu C_D Re}{24\rho_p D_p^2}(u_i - u_p) + \frac{g(\rho_p - \rho)}{\rho_p} + F \tag{8}$$

$$Re = \frac{\rho d_p |u_p - u|}{\mu} \tag{9}$$

$$C_D = \alpha_1 + \frac{\alpha_2}{Re} + \frac{\alpha_3}{Re^2} \tag{10}$$

where u_p denotes the particle velocity, $m \cdot s^{-1}$; u_i is the fluid-phase velocity, $m \cdot s^{-1}$; μ is the molecular viscosity of the background phase, Pa·s; ρ_p is the density of particles, $kg \cdot m^{-3}$; ρ is the fluid-phase density, $kg \cdot m^{-3}$; D_p is the diameter of solid particles, mm; C_D is the drag coefficient; Re is the Reynolds number; F is the additional acceleration due to other forces (i.e., force/unit particle mass), $m \cdot s^{-2}$; α_1, α_2 and α_3 are constants for several ranges of Re.

All governing equations were finally solved in the commercial solver ANSYS FLUENT. The membrane surface and channel wall were considered as a solid wall with no-slip boundary condition. In the span-wise direction, a periodic boundary condition was enforced due to the symmetry of flow and the filament cell repetition. The fluid domain of the proposed spacer model was discretized into 5.8–8.1 million control volumes followed by the grid refinement process. A flow velocity of 0.15 $m \cdot s^{-1}$ was applied at the inlet, and the outlet was kept at a pressure value of 0.6 MPa corresponding to the filtration experiments.

Spacer performances were studied experimentally in a cross-flow module of NF filtration. The spacer and NF270 membrane were placed in the flow cell channel with a height of 1.2 mm (the spacer thickness). Peristaltic pumps (EC-304-200B, Sanjiaozhou, China) were used to circulate the feed solution at an initial velocity of 0.15 $m \cdot s^{-1}$ (flow rate = 378 $mL \cdot min^{-1}$) in physical cleaning process, using secondary effluents suspended with 0.1 $mg \cdot L^{-1}$ NPs (80 nm) as influent. The experiments were carried out at an outlet constant pressure of 0.6 MPa, with two digital pressure gauges placed at the feed inlet and outlet, respectively. The permeate flux, flux recovery and EPS contents on the membrane and spacer surface were measured to assess the performance of the perforated column spacers.

3. Results and discussion

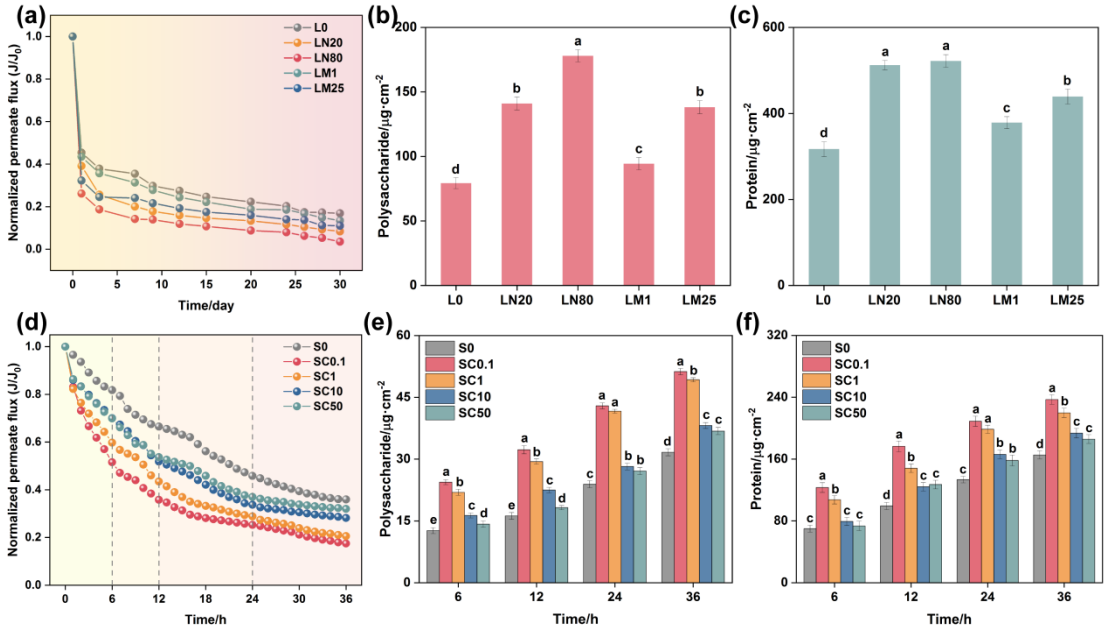
3.1 Effects of MNPs on membrane biofouling formation

Long-term experiments (30-days) were performed in parallel to compare the

size-dependent effects of MNPs (20 nm–25 μm) on membrane biofouling characteristics (Fig. 2a). The normalized permeate flux decreased rapidly in the initial 36 h, followed with a more gradual further decline. Nanoplastics, especially the 80 nm NPs exhibited the strongest effects, and the relative permeate flux decline for all the tests was as follows: LN80 > LN20 > LM25 > LM1 > L0, after 30 days filtration. Exploring the interaction variability at temporal scales throughout the biofilm development helps to understand comprehensively the succession dynamics and biological interactions of multispecies biofilms (Yuan et al., 2021). We divided the first 36 h of rapid flux decline into four stages, and further analyzed the concentration-dependent effects of NPs (80 nm) on membrane biofouling development. In a previous work, we demonstrated that varying NPs concentrations exacerbated membrane biofouling to different extents by influencing microbial metabolisms (i.e., *Pseudomonas aeruginosa*). Specifically, low-dose NPs (0.1 $mg \cdot L^{-1}$) upregulated biofilm-related pathways (quorum sensing, energy metabolism and secretion systems), increasing polysaccharide synthesis and biofilm formation. High-dose NPs (50 $mg \cdot L^{-1}$), however, induced oxidative stress (ROS), DNA damage, and energy crisis (ATP depletion), resulting in cell lysis and cytoplasmic leakage. MNPs can cause mild membrane fouling, but their impact is very small compared to the significant effects of biofouling (Liu et al., 2024). Consistently, the presence of NPs in this work also significantly exacerbated membrane biofouling (Fig. 2d). In the absence of intentional NP addition (S0), membrane biofouling was less severe, with a normalized permeate flux of 35.9% after 36 hours of operation. The flux decline was more pronounced at

0.1–1 mg·L^{-1} NPs concentrations, with normalized permeate flux dropping to 18.5%–21.6%, even surpassing systems with higher NPs concentrations (10–50 mg·L^{-1}).

EPS form a highly hydrated gel matrix where microbes are embedded, forming a substantial barrier to flow permeation across the filtration membrane (Wang et al., 2023). To investigate the size and concentration effects of MNPs on microbial EPS secretion, the contents of polysaccharides and proteins in membrane biofouling layers were determined with time. As shown in Fig. 2b-c, different sizes of MNPs stimulated microbial EPS secretion significantly, with nanoplastics LN80 yielding the greatest polysaccharide and protein contents (2.3- and 1.6-fold of L0). In terms of the NPs concentration effects, the polysaccharide contents increased to 1.6–1.5 and 1.2–1.3 times with lower (0.1–1 mg·L^{-1}) and higher (10–50 mg·L^{-1}) concentrations of NPs treatments, respectively (Fig. 2e). Similarly, the protein content was 165.4 μg·cm^{-2} in S0 after 36 h filtration, significantly lower than the 0.1–50 mg·L^{-1} NPs treated groups (236.9–185.8 μg·cm^{-2}, $p < 0.05$, Fig. 2f). These results elucidated that MNPs stimulated microbial EPS (especially the polysaccharides) secretion, thus facilitated bacteria aggregation and aggravated membrane biofouling to resist MNPs stress. In addition, polystyrene MNPs are expected to interact with EPS and trap in the biofilm matrix due to their hydrophobic surfaces, stimulate subsequent microbial EPS secretion and accelerate membrane biofouling (Yang et al., 2024). Overall, MNPs had both size-based and concentration-based stimulative effects on microbial secretion, and 0.1 mg·L^{-1} of 80 nm NPs induced the most severe membrane biofouling.



335

336 **Fig. 2.** Normalized permeate flux over time for secondary wastewater effluent with (a)
337 different MNPs sizes (20 nm–25 μm, 0.1 mg·L^{-1}, 30 days) and (d) different NPs
338 concentrations (0.1–50 mg·L^{-1}, 80 nm, 36 h); the content of polysaccharides (b) and
339 proteins (c) in membrane biofouling layers after 30 day filtration; polysaccharide (e)
340 and protein (f) contents in membrane biofouling layers after 6, 12, 24 and 36 h
341 filtration. The lowercase letters represent statistically significant differences among
342 different groups.

343 **3.2 Change in microbial community structure driven by MNPs**

344 Different microorganisms may have different tolerances to MNPs, and the
345 microbial community structure could be the key to regulating biofilm formation and
346 development (Cai et al., 2023). The abundance and structure of bacterial communities
347 exposed to MNPs were identified from 16S rRNA gene sequences. Fig. 3a-b display
348 the Shannon and Chao indexes in biofouling layers, which are representative of the
349 community diversity and richness. After 36 h filtration, the values of Chao and

Shannon indexes were the highest under 0.1–1 mg·L^{-1} NPs exposure, followed by the 10–50 mg·L^{-1} NPs treatments and the control (S0), indicating that the lower NPs concentrations more clearly stimulated the bacterial richness and diversity (Fig. 3b). For the 30 day long-term experiments, the biofilm communities under MPs exposure had significantly lower Chao and Shannon indexes, while minor differences in microbial richness and diversity were observed between NPs treatment groups and the control (L0, Fig. 3a). Overall, microbial richness and diversity increased after short-term NPs exposure (especially at 0.1–1 mg·L^{-1} NPs concentrations), but decreased subsequently with prolonged MNPs stress compared to the control.

The microbial community compositions at the phylum level indicated that the taxonomic composition was significantly altered by MNPs (Fig. 3c-d). Proteobacteria and Bacteroidota were the two dominant phyla under MNPs exposure. Among them, the relative abundance of Bacteroidota increased by 43.3%–56.9% and 23.9%–39.6% under lower (0.1–1 mg·L^{-1}) and higher (10–50 mg·L^{-1}) concentrations of NPs exposure, respectively (Fig. 3d). The microplastic-degrading bacterial species in Proteobacteria can produce cellulose as a molecular glue to enhance the biofilm integrity (Wolf-Baca and Siedlecka, 2023). Another key phyla, Bacteroidetes, is capable of converting proteins and carbohydrates to short-chain fatty acids and promoted the biofilm assembly in the early stage (Fu et al., 2018; Mercado et al., 2022).

At genus levels, the relative abundance of *Acinetobacter*, *Asticcacaulis* and *Novosphingobium* were generally increased under MNPs exposure (Fig. S3). As the most dominant genus (22.1%–46.0%) after 36 h filtration, *Acinetobacter* is well known

372 to adhere to, and form, biofilms on biotic and abiotic surfaces (Kim et al., 2023; Nouha
373 et al., 2016). The Mantel test revealed significant associations between the microbial
374 community and the levels of polysaccharides and proteins in biofouling layers, with
375 higher Mantel's *r* values reflecting stronger associations and lower *p* values signifying
376 greater statistical significance (Guan et al., 2024; Li et al., 2024; Zhang et al., 2022)
377 (Fig. 3e). *Novosphingobium*, *Legionella*, *Asticcacaulis* and *Rhodovarius* were
378 identified as keystone species that exhibited significant positive correlations with the
379 polysaccharide and protein contents (Mantel's $p \leq 0.05$). *Novosphingobium* is a
380 potential polystyrene degradation species to colonize on MPs surfaces, with
381 polystyrene as a carbon and energy source, and is considered to have a high tolerance to
382 MNPs cytotoxicity due to its strong stress adaptation to adverse environments (e.g.,
383 heavy metals and ore tailing contamination) (Liu et al., 2023a; Pan et al., 2021; Reis et
384 al., 2020). *Legionella* survives in harsh or bactericidal environmental conditions (e.g.,
385 excessive heat and chlorine) by associating with amoebae and secreting a myriad of
386 effector proteins (Mondino et al., 2020; Salinas et al., 2021), whereas *Asticcacaulis*
387 shows superior ability in cellulose and hemicellulose decomposition (López-Mondéjar
388 et al., 2020; Nguyen et al., 2019). Therefore, this highlighted the enrichment of
389 MNPs-tolerant, hypermetabolic and polystyrene-degradable genera under MNPs
390 exposure, which further strongly facilitated microbial EPS secretion, and aggravated
391 membrane biofouling.

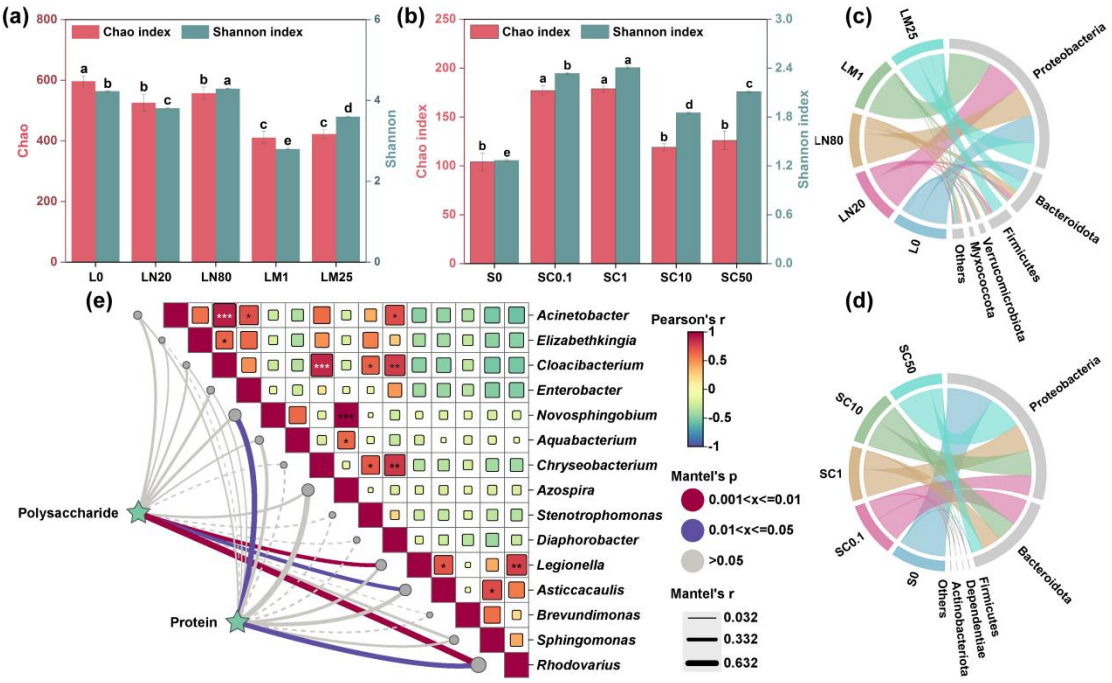


Fig. 3. Shannon and Chao indices of microbial communities exposed to: (a) 20 nm–25 μm MNPs (0.1 mg·L^{-1}) after 30 days of filtration, and (b) 80 nm NPs (0.1–50 mg·L^{-1}) after 36 h of filtration, the error bars show standard deviations based on triplicate measurements for each experimental condition. Relative abundance of bacterial phyla exposed to (c) 20 nm–25 μm MNPs (0.1 mg·L^{-1}, 30 days) and (d) 0.1–50 mg·L^{-1} NPs (80 nm, 36 h). Correlation analysis of microbial community composition and EPS contents (i.e., polysaccharides and proteins) by the Mantel test (e): pairwise correlations among genera are displayed in the triangular region, with a color gradient representing Pearson correlation coefficients. The width of the connecting lines indicates the strength of the correlation (Mantel's *r*), while the edge color reflects statistical significance (Mantel's *p*). Solid and dashed lines denote positive and negative associations, respectively.

3.3 Change in co-occurrence networks driven by MNPs

Uncovering the symbiotic relationships among species in microbial communities

is essential for understanding the biofilm formation process, identifying keystone species and elucidating the variation of potential biotic interactions in microbial communities (Fig. 4a-b). The long-term community network (20 nm–25 μm, 0.1 $mg \cdot L^{-1}$, 30 day) was composed of 334 nodes and 1067 edges, whereas the short-term counterpart (0.1–50 $mg \cdot L^{-1}$, 80 nm, 36 h) consisted of 191 nodes and 747 edges, suggesting an increasing network size and complexity with biofilm development and MNPs stress. A similar modularity (0.89–0.84) was observed in the biofilm community network of long-term experiments (20 nm–25 μm, 0.1 $mg \cdot L^{-1}$, 30 day) and short-term experiments (0.1–50 $mg \cdot L^{-1}$, 80 nm, 36 h), indicating the highly enough microbial network functions, stability and robustness after 36 h NF filtration (Mercado et al., 2022). Of note, the short-term bacterial network showed a much higher proportion of positive correlations (95.4%) than that of long-term groups (67.3%), implying the dominating co-occurrence relationship induced a rapid biofilm formation and flux reduction in the initial 36 h (Fig. 2a). Hub microorganisms (i.e., nodes highly connected to other members) represent keystone species that regulate the microbial co-occurrence network (Chen et al., 2022). *Legionella* showed the greatest influence on the long-term network structure, whereas *Acinetobacter* and *Novosphingobium* had the most links with neighboring genera in the short-term community network. These genera with the greatest connectivity promoted microbial EPS secretion through symbiosis and were required to maintain a stable microbial community. Overall, these results emphasized the MNPs regulations on modular structure and keystone taxa with membrane biofilm community network development via the involvement of interspecific interactions.

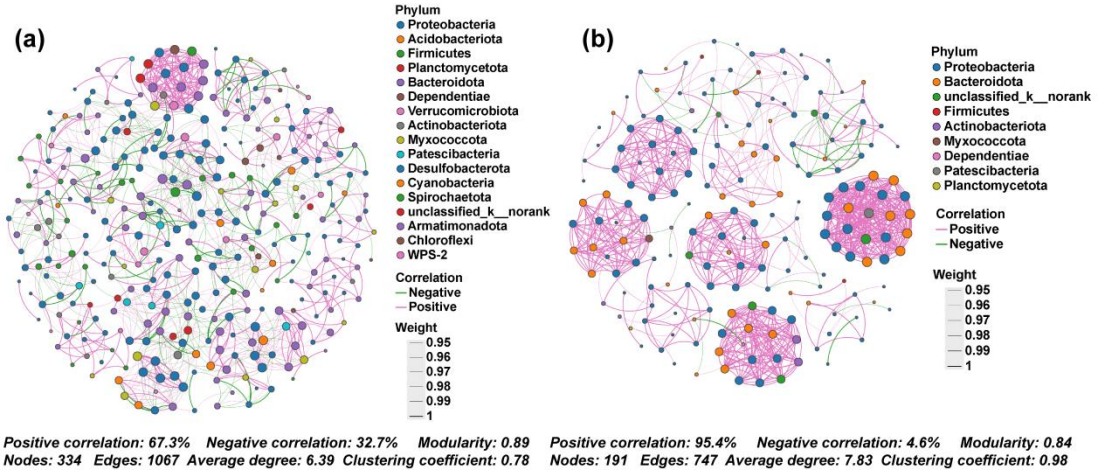


Fig. 4. Co-occurrence network analysis of microbial communities (a) under size-dependent MNPs exposure (20 nm–25 μm, 0.1 mg·L^{-1}, 30 day) and (b) under concentration-dependent NPs exposure (0.1–50 mg·L^{-1}, 80 nm, 36 h); edges represent Spearman's correlation relationships, only resulting correlations with a *p*-adjust (BH) < 0.01 and Spearman's |r| ≥ 0.7 are included; different colors represent different phylum, the node diameter increases with the number of direct neighbors; the pink and the green lines suggest positive and negative correlations, respectively.

3.4 Change in metabolic pathways and community functions driven by MNPs

The relative abundance of pathways (RAPs) annotated by the Kyoto Encyclopedia of Genes and Genomes (KEGG) were revealed to evaluate the changes in the microbial metabolic process (Table S4). At 0.1–1 mg·L^{-1} (SC0.1&SC1 *vs.* S0) and 10–50 mg·L^{-1} (SC10&SC50 *vs.* S0) of 80 nm NPs exposure (Fig. 5a-b), functional pathways that are relevant to glycan biosynthesis and metabolism, ko00572 (Arabinogalactan biosynthesis–Mycobacterium), ko00531 (Glycosaminoglycan degradation), ko00604 (Glycosphingolipid biosynthesis–ganglio series), ko00603 (Glycosphingolipid biosynthesis–globo and isoglobo series), ko00571

(Lipoarabinomannan biosynthesis), ko00540 (Lipopolysaccharide biosynthesis), ko00511 (Other glycan degradation) and ko00513 (Various types of N-glycan biosynthesis), were significantly upregulated ($Log_2FC > 1$). The glycosphingolipid (GLS) was reported to be a key player in the bacterial attachment and permanent fouling of NF membranes, due to its irreversible interaction with membrane surfaces (Haas et al., 2015). Arabinogalactan (AG) and lipoarabinomannan (LAM) are two major cell envelope glycans and cell wall components, which make significant contributions to microaggregate and biofilms structural integrity (Palceková et al., 2019). Therefore, the promoted microbial cell surface glycans biosynthesis under NPs exposure was vital for bacterial adhesion and biofilm formation.

In comparison, two cell motility related pathways, ko02040 (Flagellar assembly) and ko02030 (Bacterial chemotaxis), were significantly downregulated under 0.1–50 $mg \cdot L^{-1}$ NPs exposure (80 nm). The flagellar assembly and bacterial chemotaxis are closely related to biofilm initial colonization and biofilm dispersion on the membrane surface. Specifically, the bacterial chemotaxis system modulates cell motility to enhance the acquisition of high-value nutrients such as amino acids or sugars, providing optimal conditions for bacterial growth and thus facilitates the initiation of biofilm formation (Colin et al., 2021; Guttenplan and Kearns, 2013). After that, the expression of genes required for swimming motility are generally repressed to reduce the cellular resource and energy budget consumption, thus promoting formation of larger and more structured biofilms (Fig. 5f). Therefore, the repressed bacterial chemotaxis inhibited the reactivation of cell motility, which further promoted the

development of stabilized three-dimensional architectural biofilms and suppressed the biofilm dispersal. Overall, the upregulated pathways of glycan biosynthesis and metabolism induced significantly greater polysaccharide contents in biofilms under NPs exposure (80 nm, 36 h, 0.1–50 $mg \cdot L^{-1}$), whereas the suppressed bacterial flagellar synthesis and motility further reduced energy expenditure to cope with adverse environments, as well as facilitating the transformation from active cells to stationary biofilm cells.

The relative abundance of 122 pathways were significantly upregulated while only 21 pathways were downregulated in L0 *vs.* S0, indicating enhanced community functions with the evolution of membrane biofouling (Fig. 5c). Seventeen signal transduction related pathways were motivated in L0 *vs.* S0, which are important to maintain microbial metabolic homeostasis and promote intercellular communications (Pang et al., 2023). In comparison, the relative abundance of 75 pathways were significantly downregulated whereas just 8 pathways were upregulated under long-term NPs exposure (LN20&LN80 *vs.* L0), mainly due to the strong cytotoxicity effect of NPs (Fig. 5d). Minor differences of RAPs were detected between long-term MPs treatments and the control (LM1&LM25 *vs.* L0, Fig. 5e), with merely 10 upregulated pathways and 19 downregulated pathways, suggesting that MPs has less effect on bacterial activity than NPs due to its larger sizes (Liu et al., 2024). Four pathways of cell growth and death (ko04111, ko04110, ko04114 and ko04218) were inhibited in LN20&LN80 *vs.* L0, indicating the inhibition of bacterial proliferation. Two O-glycan biosynthesis pathways (i.e., ko00514 and ko00512) were upregulated

under NPs exposure (20–80 nm, 0.1 $mg \cdot L^{-1}$, 30 day), which promoted the microbial aggregation, surface adhesion, and were considered to be an important self-protection strategy against NPs stress. In MPs systems (1–25 μm, 0.1 $mg \cdot L^{-1}$, 30 day), glycosphingolipid and glycosaminoglycan biosynthesis pathways were significantly upregulated (i.e., ko00603, ko00604, ko00533 and ko00534). Glycosphingolipids were reported to exhibited 50% stronger adhesion to reverse osmosis membranes than EPS alone (Gutman et al., 2014). The combined presence of glycosphingolipid (known to enhance adhesion) and EPS contributed to the structural integrity of membrane biofilm matrix. Additionally, glycosaminoglycans (heteropolysaccharides containing hexosamine and uronic acid or galactose) are key components of microbial surfaces, providing high charge density and structural support of extracellular matrix (Felz et al., 2020). These differences suggest that MPs and NPs trigger distinct microbial responses, potentially due to variations in particle size and surface interactions.

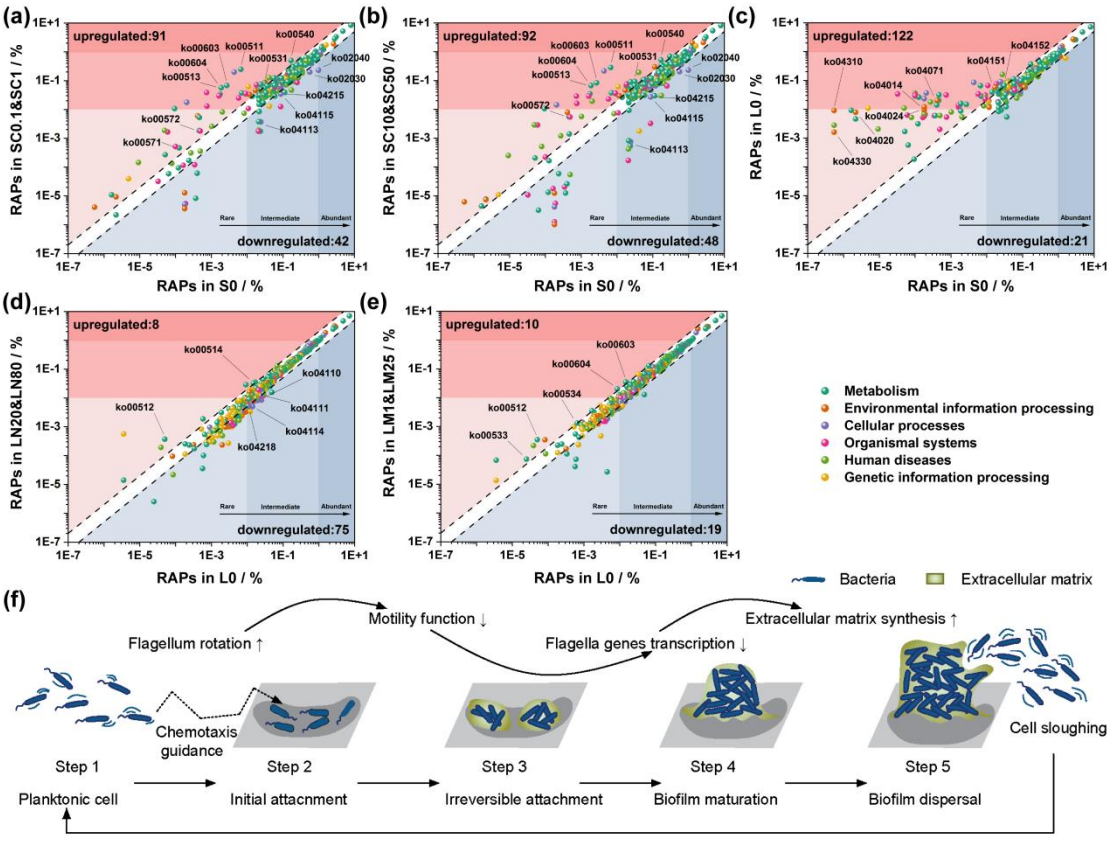


Fig. 5. Relative abundance distribution of the total pathways by KEGG annotation, SC0.1&SC1 *vs.* S0 (36 h, a), SC10&SC50 *vs.* S0 (36 h, b), L0 *vs.* S0 (30 days *vs.* 36 h, c), LN20&LN80 *vs.* L0 (30 days, d) and LM1&LM25 *vs.* L0 (30 days, e). The relative abundance of functions was converted into an exponential form. Upregulated ($Log_2FC > 1$) and downregulated ($Log_2FC < -1$) points were shown in red and blue shaded areas, respectively. Transparency was adopted to distinguish the relative abundance of pathways (RAPs) in three degrees (i.e., Abundant ≥ 1%, 0.01% < Intermediate < 1% and Rare ≤ 0.01%). Key steps involved in functional biofilms formation (f). Firstly, chemotaxis guides bacteria to swim toward nutrients and abiotic surfaces. After that, cells proliferate in the monolayer and nascent clusters form, accompanied by the inhibition of flagella genes transcription. Then, the biofilm matures into a thickness of several layers with the accumulation of extracellular matrix. Lastly, the biofilm

disperses with cells sloughing, and the biofilm life cycle reverts to the origin.

3.5 Key enzyme abundance and GSEA analysis of microbial metabolism

As an important component of bacterial outer membranes, lipopolysaccharide (LPS) contains negatively charged lipids and long chain polysaccharides with plentiful hydroxyl groups (Si et al., 2023). Key procedures of LPS biosynthesis are shown in Fig. S4a. Most likely as a response to resist the toxicity of MNPs, the relative abundance of key enzymes related to LPS biosynthesis generally increased under MNPs exposure, especially in NPs-added groups of SC0.1 and SC1 (Fig. 6a). Microbial biosynthesis and secretion of exopolysaccharides were involved in mediating the structural transitions of biofilms, leading to subsequent cell aggregation and membrane biofouling formation (Bernal-Bayard et al., 2023; Charlton et al., 2023). Stress related to 0.1–1 $mg \cdot L^{-1}$ of NPs was also found to stimulate bacterial functional potentials including exopolysaccharide production (e.g., ExoX, ExoY, ExoQ and ExoZ) and exopolysaccharide biosynthesis (e.g., ExoF and ExoP) most significantly. QS is a bacterial communication process that enables microorganisms to coordinate collective behaviors by sensing cell density and modulating gene expression accordingly (Bodelón et al., 2016; Zhang et al., 2019). The acyl-homoserine lactones (AHLs) based QS system regulates critical microbial social behaviors, including virulence expression, exoenzyme production, swarming motility and biofilm formation (Yan et al., 2021). MNPs upregulated the relative abundance of functional enzymes (e.g., PhzF, TraR, MexI and CiaH/R) involved in synthesizing AHL signaling molecules, specifically N-Hexanoyl-L-homoserine lactone (C6-HSL) and

539 N-(3-Oxopentanoyl)-L-homoserine lactone (3-oxo-C6-HSL). The regulating effects of
540 3-oxo-C8-HSL and C6-HSL on increasing biomass growth rates, microbial activity
541 and extracellular protein production have been widely verified in previous works (Li et
542 al., 2015; Tan et al., 2014; Yan et al., 2021). Thus, the high upregulation of LPS and
543 exopolysaccharide biosynthesis and quorum sensing related enzymes stimulated
544 microbial polysaccharides secretion and caused the most severe membrane biofouling.
545 KEGG pathway enrichment analyses were also performed to identify key
546 enzymes enhancing bacterial amino acid biosynthesis and metabolism against MNPs
547 presence. The key pathways of tyrosine metabolism, cysteine and methionine
548 metabolism, and alanine, aspartate and glutamate metabolism, are shown in Fig. S4b-c.
549 The results suggested that the tyrosine metabolism pathway was upregulated more
550 significantly when exposed to lower NPs concentrations (Fig. 6e). Specifically, the
551 relative abundance of tyrosinase (TYR, Log_2FC = 5.6–6.4), phenylacetaldehyde
552 dehydrogenase (FeaB, Log_2FC = 3.8–4.0) and monoamine oxidase (MAO, Log_2FC =
553 2.1–2.4) were remarkably increased by exposure to 0.1–1 $mg \cdot L^{-1}$ NPs. For the effects
554 of size-dependent MNPs, the metabolism of alanine, aspartate, glutamate, cysteine
555 and methionine were motivated, especially by NPs exposure (Fig. 6f). The relative
556 abundance of homocysteine S-methyltransferase (MmuM, Log_2FC = 1.3–1.4),
557 S-ribosylhomocysteine lyase (LusX, Log_2FC = 1.8–3.3), homocysteine
558 S-methyltransferase (AspQ, Log_2FC = 1.7–1.9) and aspartate 4-decarboxylase (AsdA,
559 Log_2FC = 1.1–2.4) were significantly upregulated in the LN20 and LN80 tests.
560 Overall, MNPs regulated microbial secretions in different pathways, and these amino

561 acid metabolic pathways contributed to higher bacterial protein secretions in the
562 presence of MNPs.

563 Gene expression results of bacterial secretion system, biosynthesis of amino acid
564 and glycan biosynthesis pathways were further interpreted via gene set enrichment
565 analysis (GSEA, Fig. S5), based on the metagenomic sequencing of 89 *Acinetobacter*
566 species (Table S5). Gene set enrichment for bacterial secretion system (NES = 0.821),
567 biosynthesis of amino acid (NES = 1.081) and glycan biosynthesis (NES = 1.171) in
568 MNPs treatment groups *vs.* the control group, yielded positive normalized enrichment
569 scores (NES), indicating the generally upregulated expression of genes involved in
570 those three pathways exposed to MNPs, consistent with higher polysaccharide and
571 protein contents detected in membrane biofilms (Fig. 2). Negative normalized
572 enrichment scores (-0.679, -0.995 and -0.984) of bacterial secretion system,
573 biosynthesis of amino acid and glycan biosynthesis pathways, were observed in MPs *vs.*
574 NPs treatment groups, suggesting higher microbial secretion ability under NPs
575 exposure than that under MPs exposure (Table S6). Overall, the stimulated biofilm
576 formation functions (e.g., amino acid and glycan biosynthesis) under MNPs exposure
577 promoted microbial protein and polysaccharide metabolism and led to severe
578 membrane biofouling.

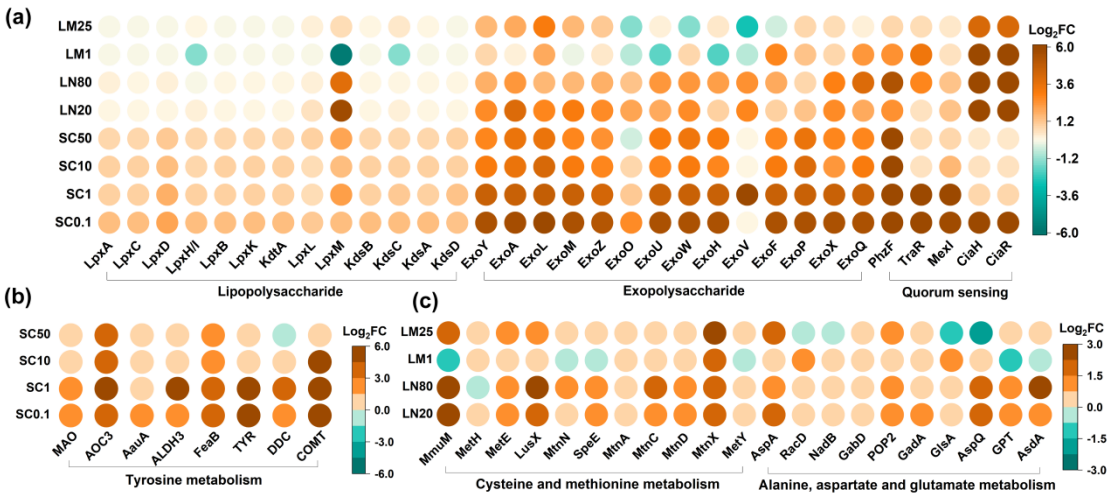


Fig. 6. Relative abundance of functional enzymes related to the lipopolysaccharide, exopolysaccharide biosynthesis and quorum sensing (36 h and 30 days, a), tyrosine metabolism (36 h, b) and alanine, aspartate, glutamate, cysteine and methionine metabolism (30 days, c). The quantification of enzymes are expressed as the log_2-transformed fold changes relative to controls.

3.6 Hydrodynamics of feed channels based on the CFD-DPM modeling

Spacer modification is an important method to promote fluid mixing and enhance mass transfer inside feed channels, thus mitigating membrane biofouling by reducing MNPs deposition and microbial adhension (Lin et al., 2021). Three types of spacers, specifically, a stand spacer (SS), and a perforated column spacer with hole diameters of 0.5 mm (PCS_0.5) and 0.3 mm (PCS_0.3), were designed and fabricated by 3D-printer technology. The hydrodynamic characteristics of feed channels with the three feed spacers were systematically studied, and the spatial and transient distribution of fluid-dynamic parameters were investigated. Fig. 7a shows a comparison of the simulated fluid pressure at the central plane x-y (1/2 height of the z-axis) and plane x-z (1/2 height of the y-axis) in the presence of SS, PCS_0.5 and

PCS_0.3. The perforated column spacer caused a much lower pressure drop and pumping energy consumption, due to its larger flow channel porosity (Fig. 7g, 85.4% for PCS_0.5, 84.4% for PCS_0.3 and 69.3% for SS). Specifically, the fluid pressure declines along the channel length of SS (0.979 mbar/mm) were nearly 6 and 1.2 times of the column spacer and the perforated spacer reported eariler, while these values were increased to nearly 9 times for PCS_0.5 (0.108 mbar/mm) and PCS_0.3 (0.120 mbar/mm, Fig. 7d) (Ali et al., 2019; Kerdi et al., 2018).

As shown in Fig. 7b, the flow velocity contours at the central plane x-y and plane x-z exhibited periodic distribution patterns over the whole channel volume. For the SS case, the filament nodes obstructed the incoming feed flow, serving as supporting bases to separate the tightly placed membranes. Therefore, the downstream side of filament nodes exhibited the lowest local velocity and generated a large area of stagnant zones. The contaminants had a high deposition tendency in these dead zones, which further facilitated membrane fouling. As spacer holes were introduced, the local velocity magnitude increased significantly as the fluid passed through filament holes, which not only eliminated the dead zones, but also swept away the contaminants behind the filament intersection. In case of PCS_0.5, the average velocities of plane x-y and plane x-z were 1.29 and 1.25 times of SS, whereas, for PCS_0.3 it reached merely 1.02 and 0.79 times, respectively. Therefore, the introduction of holes disturbed the potential fouling zones behind the nodes with a diameter of 0.5 mm, but this advantage reduced as the hole diameter decreased.

To evaluate the potential effect of the three spacer geometries on fouling patterns,

CFD-DPM modeling was conducted to predict the streamlines of fluid element paths and the particle trajectory, overlapped with velocity magnitude contours (Fig. 7c). For all geometries, the lowest velocity of streamlines was mainly located behind the nodes (dead zones), while the highest values were distributed in narrow flow sections between filaments and the membrane (constriction zones) and inside the holes. The relatively stagnant zones downstream of PCS_0.5 and PCS_0.3 were less extensive than for the SS due to the introduced holes and thin cross-connected spacer filaments, which in turn led to enhanced mass transfer and micro-jets downstream of the filament. These micro-jets induced a larger extent of boundary layer disruption and enhanced mass transfer performance. Additionally, the particle transport and deposition simulations showed that the MNPs particles passed through the perforated holes at greater speeds, leading to less foulant accumulation. On the vertical cross-sectional plane (plane x-z) of feed channels, the wake behind cylindrical nodes of PCS_0.5 and PCS_0.3 showed more significant oscillations than SS. Therefore, from the theoretical findings of hydrodynamics in the presence of SS, PCS_0.5 and PCS_0.3, it can be concluded that PCS structures played a significant beneficial role in terms of increasing mass transfer performance and mitigating foulant deposition, compared to the SS arrangement. The hydrodynamic enhancements were achieved by introducing horizontal holes in column spacers, which combined the advantages of columnar spacers and perforated spacers (e.g., increased micro-jets and fluid velocity, reduced pressure drop and less energy consumption).

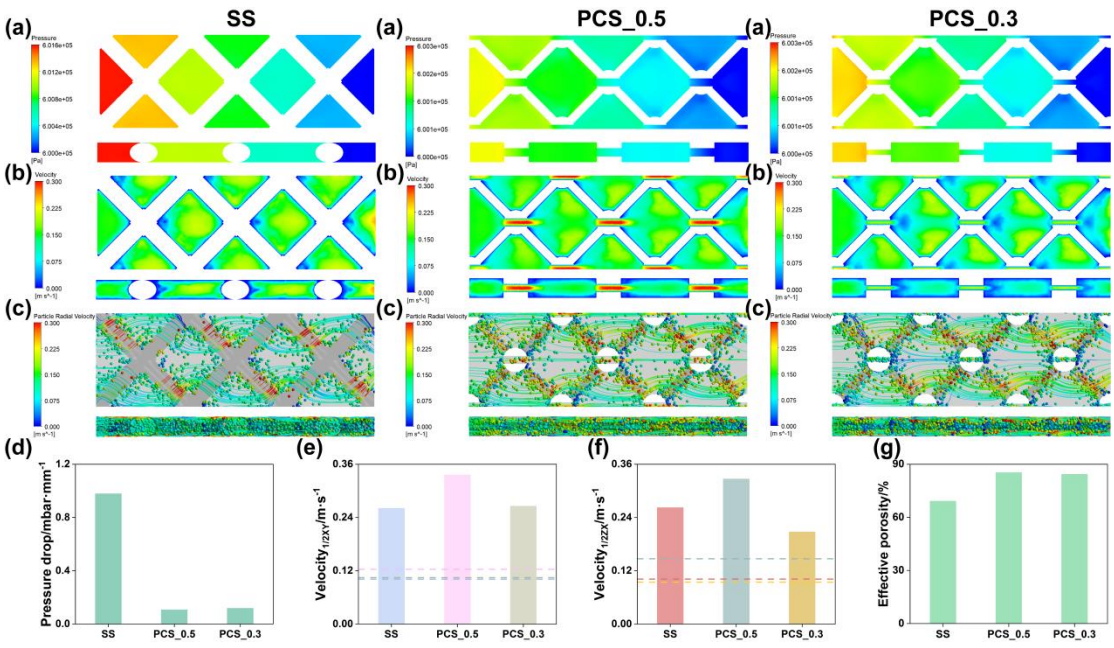


Fig. 7. Spatial distribution of numerically simulated fluid pressure (a) and velocity (b) at the central plane x-y and plane x-z of feed channels. Streamline and particle trajectory (c), theoretically estimated pressure drop (d), maximum local (columns) and average (dotted lines) velocity in plane x-y (e) and plane x-z (f), and effective porosity of feed channels (g) for the different types of spacers (SS, PCS_0.5 and PCS_0.3).

3.7 Mitigation effects of modified spacers on membrane biofouling with NPs stress

The wall shear stress at membrane surfaces can be enhanced by physical cleaning to partially dislodge MNPs particles and foulants, and thus mitigate the decrease in membrane flux (Enfrin et al., 2021). To investigate the effects of NPs concentrations (0–50 mg·L^{-1}, 80 nm, Fig. 8a) and modified spacers (Fig. 8c) on membrane biofouling in the treatment of real secondary effluent, periodic physical cleaning was conducted. Supportive analysis in terms of total filtration resistance including physically irreversible fouling ratio (FR_{ir}), and physically reversible fouling ratio (FR_r), was

654 further conducted (Fig. S6). After 5 operating cycles, the feed solutions containing
655 0.1–1 mg·L^{-1} NPs presented the lowest flux recovery ratio (FRR, 48.5%–52.3%),
656 followed by the 10–50 mg·L^{-1} NPs solutions (61.5%–64.7%) and the control solution
657 (76.7%, Fig. 8b). The FR_{ir} under NPs exposure was 1.4–2.2 times that of the control
658 group. Lower FRR and higher FR_{ir} values indicated that the foulants are more difficult
659 to remove from the membrane surface or pores, since the enhanced secretion of
660 strongly attached polysaccharides and hydrophobic proteins accelerated the adhesion
661 effect between biofilms and the membrane surface. Overall, NPs aggravated
662 membrane biofouling severely even with the intervention of physical cleaning.

663 The quantitative comparison of numerical and experimental results is necessary to
664 evaluate the potential fouling mitigation ability of geometric modified spacers, and to
665 strengthen the assessment for practical spacer applications. The performance of three
666 types of spacer in terms of fouling potentials, permeate flux and flux recovery in
667 physical cleaning cycles were tested experimentally to support the theoretical findings
668 from CFD analyses (Fig. 8c). In accordance with the simulated data, a much milder flux
669 decline was experienced in the presence of the perforated column spacer, with
670 PCS_0.5 obtaining the highest permeate flux. In addition, FR_{ir} and FR_r were reduced
671 by 6.0%–13.1% and 5.8%–10.0%, respectively, in the presence of perforated column
672 spacers, compared with the standard spacer (Fig. 8d-e). Biofilm development was
673 observed by analyzing the accumulated biomass (polysaccharide and protein contents)
674 on the membrane and spacer surface at the end of the study (Fig. 8f-i). Compared to
675 SS, PCS_0.5 reduced polysaccharide and protein contents by up to 30.0%–39.8% and

20.5%–40.8%, respectively, on the spacer and membrane surface. These results indicated that the perforated column design significantly lowered fouling on the membrane and spacer surface by optimizing the hydrodynamics of spacer-filled channels, which contributed to the long-term stable operation of the membrane system.

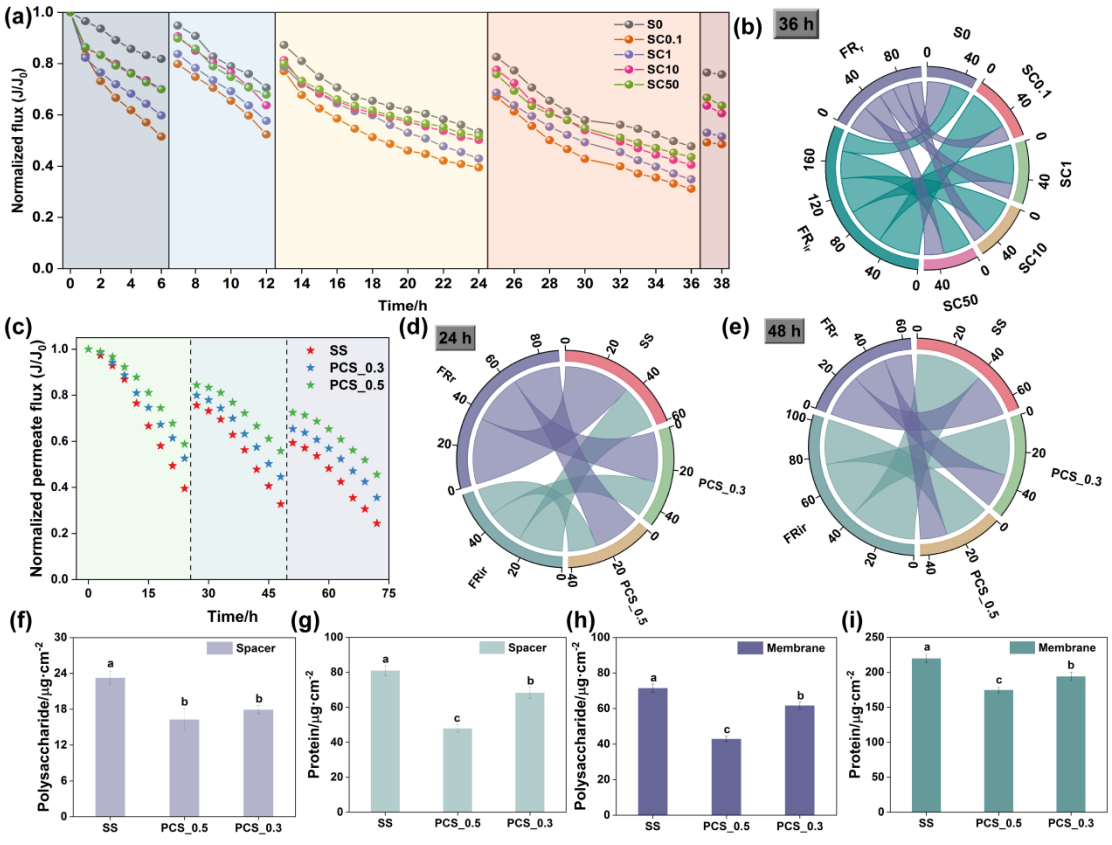


Fig. 8. Normalized flux as a function of the fouling time after periodic physical cleaning under 0–50 mg·L^{-1} 80 nm NPs exposure (without feed spacer) (a); the proportion of FR_{ir} (%) and FR_r (%) after 36 h cyclic physical cleaning (b). Normalized flux as a function of the fouling time after periodic physical cleaning in the presence of three spacers with 0.1 mg·L^{-1} 80 nm NPs in feed water (c); the proportion of FR_{ir} (%) and FR_r (%) after 24 h (d) and 48 h (e) cyclic physical cleaning; polysaccharide and protein contents on the spacer (f-g) and membrane (h-i) surface after 72 h filtration.

4. Environmental implications and conclusions

With increasing MNPs entering sewers due to human activities, NF will become an important technology to ensurethe effective interception of MNPs and public health protection. Whether, and how, MNPs particles influence microorganisms, particularly the fouling-causing organisms, and their metabolic products on membrane surface is of concern. In this study, mechanisms governing the size-dependent and concentration-dependent influences of MNPs on bacterial colonization and community succession in NF system were explored. Additionally, new types of perforated column spacer was developed to mitigate membrane biofouling and reduce energy consumption during NF process by improving the hydrodynamic characteristics of feed channels.

Compared with MPs, 0.1–1 $mg \cdot L^{-1}$ NPs stimulated bacterial glycan (e.g., arabinogalactan, glycosphingolipid, lipoarabinomannan, lipopolysaccharide and exopolysaccharide) and amino acid (e.g., tyrosine, alanine, aspartate, glutamate, cysteine and methionine) biosynthesis more significantly, while two biofilm dispersion pathways (i.e., flagellar assembly and bacterial chemotaxis) were repressed. Several genera with stronger biofilm formation and polystyrene-degrading capacity such as *Acinetobacter*, *Asticcacaulis* and *Novosphingobium* contributed to severe membrane biofouling in the presence of MNPs, thus negatively affecting the cost and efficiency of the NF process. Perforated column spacers enhanced the hydrodynamic characteristics of the membrane process by reducing the pressure drop by nearly 90% and increasing the flow velocity 1.25–1.29 times inside feed channels, which further

exhibited excellent anti-fouling performances and achieved higher flux recovery after cyclic physical cleaning. To facilitate the practical application of spacer design, future studies should prioritize advancing 3D printing technologies to achieve faster production speeds and reduce manufacturing costs. Concurrently, optimizing spacer properties (e.g., flexibility, mechanical strength, and chemical stability) will be critical to ensure their durability under operational conditions. These findings enhanced our fundamental understanding of MNPs-induced membrane biofouling and highlighted the need for WWTPs to improve performance of MNPs removal in pretreatment processes.

Acknowledgments

This work was supported by National Natural Science Foundation of China (Grant No. 52070018) and National Key Research and Development Program of China (Grant No. 2021YFC3201403).

References

Ali, S.M., Qamar, A., Kerdi, S., Phuntsho, S., Vrouwenvelder, J.S., Ghaffour, N. and Shon, H.K. 2019. Energy efficient 3D printed column type feed spacer for membrane filtration. Water Res. 164, 11.

Bernal-Bayard, J., Thiebaud, J., Brossaud, M., Beaussart, A., Caillet, C., Waldvogel, Y., Travier, L., Létoffé, S., Fontaine, T., Rokbi, B., Talaga, P., Beloin, C., Mistretta, N., Duval, J.F.L. and Ghigo, J.M. 2023. Bacterial capsular polysaccharides with antibiofilm activity share common biophysical and electrokinetic properties. Nat. Commun. 14(1), 11.

Bodelón, G., Montes-García, V., López-Puente, V., Hill, E.H., Hamon, C., Sanz-Ortiz, M.N., Rodal-Cedeira, S., Costas, C., Celiksoy, S., Pérez-Juste, I., Scarabelli, L., La Porta, A., Pérez-Juste, J., Pastoriza-Santos, I. and Liz-Marzán, L.M. 2016. Detection and imaging of quorum sensing in Pseudomonas aeruginosa biofilm communities by surface-enhanced resonance Raman scattering. Nature Materials 15(11), 1203-1211.

738 Cai, W.W., Cai, L.N., Zhao, J. and Yao, H. 2023. Prokaryotic community interchange between distinct
739 microhabitats causes community pressure on anammox biofilm development. Water Res. 233,
740 9.
741 Charlton, S.G.V., Bible, A.N., Secchi, E., Morrell-Falvey, J.L., Retterer, S.T., Curtis, T.P., Chen, J.J. and
742 Jana, S. 2023. Microstructural and rheological transitions in bacterial biofilms. Adv. Sci.
743 10(27), 10.
744 Chen, H.Z., Zhang, S.H., Lv, X., Guo, S.Z., Ma, Y., Han, B. and Hu, X.R. 2022. Interactions between
745 suspended sediments and submerged macrophytes-epiphytic biofilms under water flow in
746 shallow lakes. Water Res. 222, 12.
747 Colin, R., Ni, B., Laganenka, L. and Sourjik, V. 2021. Multiple functions of flagellar motility and
748 chemotaxis in bacterial physiology. Fems Microbiol. Rev. 45(6), 19.
749 Cui, L., Chen, P.Y., Zhang, B.F., Zhang, D.Y., Li, J.Y., Martin, F.L. and Zhang, K.S. 2015.
750 Interrogating chemical variation *via* layer-by-layer SERS during biofouling and cleaning of
751 nanofiltration membranes with further investigations into cleaning efficiency. Water Res. 87,
752 282-291.
753 Dronjak, L., Exposito, N., Rovira, J., Florencio, K., Emiliano, P., Corzo, B., Schuhmacher, M., Valero, F.
754 and Sierra, J. 2022. Screening of microplastics in water and sludge lines of a drinking water
755 treatment plant in Catalonia, Spain. Water Res. 225, 10.
756 Du, X., Mo, Z., Li, Z., Zhang, W., Luo, Y., Nie, J., Wang, Z. and Liang, H. 2021. Boron-doped
757 diamond (BDD) electro-oxidation coupled with nanofiltration for secondary wastewater
758 treatment: Antibiotics degradation and biofouling. Environ. Int. 146, 106291.
759 Dubois, M., Gilles, K.A., Hamilton, J.K., Rebers, P.A. and Smith, F. 1956. Colorimetric method for
760 determination of sugars and related substances. Anal. Chem. 28(3), 350-356.
761 Enfrin, M., Lee, J., Fane, A.G. and Dumée, L.F. 2021. Mitigation of membrane particulate fouling by
762 nano/microplastics via physical cleaning strategies. Sci. Total Environ. 788, 10.
763 Felz, S., Neu, T.R., van Loosdrecht, M.C.M. and Lin, Y. 2020. Aerobic granular sludge contains
764 Hyaluronic acid-like and sulfated glycosaminoglycans-like polymers. Water Res. 169, 115291.
765 Fu, S.F., Ding, J.N., Zhang, Y., Li, Y.F., Zhu, R., Yuan, X.Z. and Zou, H. 2018. Exposure to
766 polystyrene nanoplastic leads to inhibition of anaerobic digestion system. Sci. Total Environ.
767 625, 64-70.
768 Giagnorio, M., Ricceri, F. and Tiraferri, A. 2019. Desalination of brackish groundwater and reuse of
769 wastewater by forward osmosis coupled with nanofiltration for draw solution recovery. Water
770 Res. 153, 134-143.
771 Guan, W., Ansari, A.J., Yin, R., Qi, C. and Song, X. 2024. Optimizing feedstock organic composition
772 to regulate humification and heavy metal passivation during solid-state anaerobic digestion.
773 Chem. Eng. J. 499, 156071.
774 Gutman, J., Herzberg, M. and Walker, S.L. 2014. Biofouling of Reverse Osmosis Membranes:
775 Positively Contributing Factors of Sphingomonas. Environ. Sci. Technol. 48(23), 13941-13950.
776 Guttenplan, S.B. and Kearns, D.B. 2013. Regulation of flagellar motility during biofilm formation.
777 Fems Microbiol. Rev. 37(6), 849-871.
778 Haas, R., Gutman, J., Wardrip, N.C., Kawahara, K., Uhl, W., Herzberg, M. and Arnusch, C.J. 2015.
779 Glycosphingolipids enhance bacterial attachment and fouling of nanofiltration membranes.
780 Environ. Sci. Technol. Lett. 2(2), 43-47.

Huang, F., Zhu, Q.X., Zhou, X.D., Gou, D.Z., Yu, J.Q., Li, R.J., Tong, Z.B. and Yang, R.Y. 2021. Role of CFD based *in silico* modelling in establishing an *in vitro*-in *vivo* correlation of aerosol deposition in the respiratory tract. Adv. Drug Deliv. Rev. 170, 369-385.

Huang, S.C., Zhang, B., Zhao, Z.W., Yang, C., Zhang, B., Cui, F.Y., Lens, P.N.L. and Shi, W.X. 2023. Metagenomic analysis reveals the responses of microbial communities and nitrogen metabolic pathways to polystyrene micro(nano)plastics in activated sludge systems. Water Res. 241, 10.

Kang, S., Xue, Y.P., Lu, L., Deng, M. and Zhao, X.L. 2022. Impact and microbial mechanism of continuous nanoplastics exposure on the urban wastewater treatment process. Water Res. 223, 11.

Karakurt, C., Çelik, A.O., Yilmazer, C., Kiriççi, V. and Özyasar, E. 2018. CFD simulations of self-compacting concrete with discrete phase modeling. Constr. Build. Mater. 186, 20-30.

Kerdi, S., Qamar, A., Vrouwenvelder, J.S. and Ghaffour, N. 2018. Fouling resilient perforated feed spacers for membrane filtration. Water Res. 140, 211-219.

Kerdi, S., Qamar, A., Vrouwenvelder, J.S. and Ghaffour, N. 2021. Effect of localized hydrodynamics on biofilm attachment and growth in a cross-flow filtration channel. Water Res. 188, 116502.

Kim, B., Lee, S.W., Jung, E.M. and Lee, E.H. 2023. Biosorption of sub-micron-sized polystyrene microplastics using bacterial biofilms. J. Hazard. Mater. 458, 12.

LaRue, R.J., Patterson, B., O'Brien, S. and Latulippe, D.R. 2022. Evaluation of membrane fouling by microplastic particles in tertiary wastewater treatment processes. ACS ES&T Wat. 2(6), 955-966.

Li, A.-j., Hou, B.-l. and Li, M.-x. 2015. Cell adhesion, ammonia removal and granulation of autotrophic nitrifying sludge facilitated by N-acyl-homoserine lactones. Bioresour. Technol. 196, 550-558.

Li, D., Ping, Q., Mo, R., Guo, W., Zhang, S., Wang, L. and Li, Y. 2024. Revealing synergistic mechanisms of biochar-assisted microbial electrolysis cells in enhancing the anaerobic digestion performance of waste activated sludge: Extracellular polymeric substances characterization, enzyme activity assay, and multi-omics analysis. Water Res. 267, 122501.

Li, R.L., Zhu, L.J., Wang, Y.J. and Zhu, Y.G. 2022. Metagenomic insights into environmental risk of field microplastics in an urban river. Water Res. 223, 10.

Lin, W.-c., Shao, R.-p., Wang, X.-m. and Huang, X. 2020. Impacts of non-uniform filament feed spacers characteristics on the hydraulic and anti-fouling performances in the spacer-filled membrane channels: Experiment and numerical simulation. Water Res. 185, 116251.

Lin, W.C., Zhang, Y.T., Li, D.Y., Wang, X.M. and Huang, X. 2021. Roles and performance enhancement of feed spacer in spiral wound membrane modules for water treatment: A 20-year review on research evolvement. Water Res. 198, 23.

Liu, R.J., Zhao, S.F., Zhang, B.J., Li, G.Y., Fu, X.T., Yan, P.S. and Shao, Z.Z. 2023a. Biodegradation of polystyrene (PS) by marine bacteria in mangrove ecosystem. J. Hazard. Mater. 442, 12.

Liu, X.H., Yang, Y., Takizawa, S., Graham, N.J.D., Chen, C., Pu, J. and Ng, H.Y. 2024. New insights into the concentration-dependent regulation of membrane biofouling formation via continuous nanoplastics stimulation. Water Res. 253, 14.

Liu, X.J., Wang, S.T., Mu, L., Xie, Y.Y. and Hu, X.A. 2023b. Microplastics Reshape the Fate of Aqueous Carbon by Inducing Dynamic Changes in Biodiversity and Chemodiversity. Environ. Sci. Technol. 57(28), 10415-10425.

López-Mondéjar, R., Tláskal, V., Vetrovsky, T., Stursová, M., Toscan, R., da Rocha, U.N. and Baldrian, P. 2020. Metagenomics and stable isotope probing reveal the complementary contribution of fungal and bacterial communities in the recycling of dead biomass in forest soil. Soil Biol. Biochem. 148, 11.

Mercado, J.V., Koyama, M. and Nakasaki, K. 2022. Co-occurrence network analysis reveals loss of microbial interactions in anaerobic digester subjected to repeated organic load shocks. Water Res. 221, 11.

Mintenig, S.M., Int-Veen, I., Löder, M.G.J., Primpke, S. and Gerdts, G. 2017. Identification of microplastic in effluents of waste water treatment plants using focal plane array-based micro-Fourier-transform infrared imaging. Water Res. 108, 365-372.

Mondino, S., Schmidt, S., Rolando, M., Escoll, P., Gomez-Valero, L. and Buchrieser, C. (2020) Annual Review of Pathology: Mechanisms of Disease, Vol 15, 2020. Abbas, A.K., Aster, J.C. and Feany, M.B. (eds), pp. 439-466, Annual Reviews, Palo Alto.

Morsi, S.A. and Alexander, A.J. 1972. Investigation of particle trajectories in 2-phase flow systems. J. Fluid Mech. 55(SEP26), 193-+.

Nguyen, L.N., Nghiem, L.D., Pramanik, B.K. and Oh, S. 2019. Cometabolic biotransformation and impacts of the anti-inflammatory drug diclofenac on activated sludge microbial communities. Sci. Total Environ. 657, 739-745.

Nouha, K., Kumar, R.S. and Tyagi, R.D. 2016. Heavy metals removal from wastewater using extracellular polymeric substances produced by *Cloacibacterium normanense* in wastewater sludge supplemented with crude glycerol and study of extracellular polymeric substances extraction by different methods. Bioresour. Technol. 212, 120-129.

Ounis, H., Ahmadi, G. and McLaughlin, J.B. 1991. Brownian diffusion of submicrometer particles in the viscous sublayer. J. Colloid Interface Sci. 143(1), 266-277.

Palceková, Z., Angala, S.K., Belardinelli, J.M., Eskandarian, H.A., Joe, M., Brunton, R., Rithner, C., Jones, V., Nigou, J., Lowary, T.L., Gilleron, M., McNeil, M. and Jackson, M. 2019. Disruption of the SucT acyltransferase in Mycobacterium smegmatis abrogates succinylation of cell envelope polysaccharides. J. Biol. Chem. 294(26), 10325-10335.

Pan, H., Yang, X., Chen, H.B., Sarkar, B., Bolan, N., Shaheen, S.M., Wu, F.C., Che, L., Ma, Y.B., Rinklebe, J. and Wang, H.L. 2021. Pristine and iron-engineered animal- and plant-derived biochars enhanced bacterial abundance and immobilized arsenic and lead in a contaminated soil. Sci. Total Environ. 763, 9.

Pang, S.H., Liu, J.W., Li, T.L., Ye, K., Yan, Z.X., Zhao, L. and Bao, C.Y. 2023. Folding and unfolding of a fully synthetic transmembrane receptor for on/off signal transduction. J. Am. Chem. Soc. 145(38), 20761-20766.

Reis, M.P., Suhadolnik, M.L.S., Dias, M.F., Avila, M.P., Motta, A.M., Barbosa, F.A.R. and Nascimento, A.M.A. 2020. Characterizing a riverine microbiome impacted by extreme disturbance caused by a mining sludge tsunami. Chemosphere 253, 15.

Salinas, M.B., Fenoy, S., Magnet, A., Vaccaro, L., Gomes, T.D.S., Hurtado, C., Ollero, D., Valdivieso, E., del Aguila, C., Pozuelo, M.J. and Izquierdo, F. 2021. Are pathogenic *Legionella* non-*pneumophila* a common bacteria in Water Distribution Networks? Water Res. 196, 10.

Sarkar, D.J., Sarkar, S.D., Das, B.K., Praharaj, J.K., Mahajan, D.K., Purokait, B., Mohanty, T.R., Mohanty, D., Gogoi, P., Kumar, V.S., Behera, B.K., Manna, R.K. and Samanta, S. 2021.

Microplastics removal efficiency of drinking water treatment plant with pulse clarifier. J. Hazard. Mater. 413, 9.

Shukla, S.K., Shukla, P. and Ghosh, P. 2011. Evaluation of numerical schemes for dispersed phase modeling of cyclone separators. Eng. Appl. Comp. Fluid Mech. 5(2), 235-246.

Si, Z.Y., Li, J.G., Ruan, L., Reghu, S., Ooi, Y.J., Li, P., Zhu, Y.B., Hammond, P.T., Verma, C.S., Bazan, G.C., Pethe, K. and Chan-Park, M.B. 2023. Designer co-beta-peptide copolymer selectively targets resistant and biofilm Gram-negative bacteria. Biomaterials 294, 12.

Siddiqui, A., Lehmann, S., Bucs, S.S., Fresquet, M., Fel, L., Prest, E.I.E.C., Ogier, J., Schellenberg, C., van Loosdrecht, M.C.M., Kruithof, J.C. and Vrouwenvelder, J.S. 2017. Predicting the impact of feed spacer modification on biofouling by hydraulic characterization and biofouling studies in membrane fouling simulators. Water Res. 110, 281-287.

Song, J., Xu, D., Han, Y., Zhu, X., Liu, Z., Li, G. and Liang, H. 2023. Surface modification of FeIII-juglone coating on nanofiltration membranes for efficient biofouling mitigation. Water Res. 247, 120795.

Tan, C.H., Koh, K.S., Xie, C., Tay, M., Zhou, Y., Williams, R., Ng, W.J., Rice, S.A. and Kjelleberg, S. 2014. The role of quorum sensing signalling in EPS production and the assembly of a sludge community into aerobic granules. The ISME Journal 8(6), 1186-1197.

Toh, W., Ang, E.Y.M., Ng, T.Y., Lin, R.M. and Liu, Z.S. 2020. An investigation on the effects of nanoplastic particles on nanoporous graphene membrane desalination. Desalination 496, 10.

Toh, W., Ang, E.Y.M., Ng, T.Y., Lin, R.M. and Liu, Z.S. 2022. Antifouling bilayer graphene slit membrane for desalination of nanoplastic-infested seawater: A molecular dynamics simulation study. ACS Appl. Mater. Interfaces 14(38), 43965-43974.

Wang, H., Fan, Y.F., Zhou, M.D., Wang, W.G., Li, X. and Wang, Y.Y. 2022. Function of Fe(III)-minerals in the enhancement of anammox performance exploiting integrated network and metagenomics analyses. Water Res. 210, 11.

Wang, H., Qiu, C., Bian, S.C., Zheng, L., Chen, Y.M., Song, Y.L. and Fang, C.R. 2023. The effects of microplastics and nanoplastics on nitrogen removal, extracellular polymeric substances and microbial community in sequencing batch reactor. Bioresour. Technol. 379, 10.

Wang, P.P., Wang, F.H., Jiang, H.C., Zhang, Y.C., Zhao, M., Xiong, R.H. and Ma, J. 2020. Strong improvement of nanofiltration performance on micropollutant removal and reduction of membrane fouling by hydrolyzed-aluminum nanoparticles. Water Res. 175, 11.

Wang, Y., Wang, Z., Wang, J.X. and Wang, S.C. 2018. Triple antifouling strategies for reverse osmosis membrane biofouling control. J. Membr. Sci. 549, 495-506.

Wolf-Baca, M. and Siedlecka, A. 2023. Seasonal and spatial variations of antibiotic resistance genes and bacterial biodiversity in biofilms covering the equipment at successive stages of drinking water purification. J. Hazard. Mater. 456, 15.

Xiong, X.J., Siddique, M.S., Graham, N.J.D. and Yu, W.Z. 2022. Towards microplastics contribution for membrane biofouling and disinfection by-products precursors: The effect on microbes. J. Hazard. Mater. 426, 12.

Xu, G.F. and He, J.Z. 2022. Resilience of organohalide-detoxifying microbial community to oxygen stress in sewage sludge. Water Res. 224, 12.

Xu, R.H., Zhang, W.T., Fu, Y., Fan, F.Q., Zhou, Z.M., Chen, J.C., Liu, W.L. and Meng, F.A. 2023. The positive roles of influent species immigration in mitigating membrane fouling in membrane bioreactors treating municipal wastewater. Water Res. 235, 12.

911 Yan, H., Li, J., Meng, J., Li, J., Kumar Jha, A., Zhang, Y., Fan, Y. and Wang, X. 2021. Effects of reflux
912 ratio on the anaerobic sludge and microbial social behaviors in an expanded granular sludge bed
913 reactor: From the perspective of acyl-homoserine lactones-mediated quorum sensing. Bioresour.
914 Technol. 337, 125360.
915 Yang, Q.H., Zhang, J.J., Zhang, N., Wang, D., Yuan, X.Z., Tang, C.Y., Gao, B.Y. and Wang, Z.N. 2024.
916 Impact of nanoplastics on membrane scaling and fouling in reverse osmosis desalination
917 process. Water Res. 249, 9.
918 Yang, X.Y., He, Q., Guo, F.C., Sun, X.H., Zhang, J.M., Chen, M.L., Vymazal, J. and Chen, Y. 2020.
919 Nanoplastics disturb nitrogen removal in constructed wetlands: Responses of microbes and
920 macrophytes. Environ. Sci. Technol. 54(21), 14007-14016.
921 Ye, W.Y., Liu, H.W., Jiang, M., Lin, J.Y., Ye, K.F., Fang, S.Q., Xu, Y.D., Zhao, S.F., Van der Bruggen, B.
922 and He, Z. 2019. Sustainable management of landfill leachate concentrate through
923 recovering humic substance as liquid fertilizer by loose nanofiltration. Water Res. 157, 555-563.
924 Yuan, S.S., Xu, R.H., Wang, D.P., Lin, Q.N., Zhou, S.Y., Lin, J.Y., Xia, L.C., Fu, Y., Gan, Z.H. and Meng,
925 F.G. 2021. Ecological linkages between a biofilm ecosystem and reactor performance: The
926 specificity of biofilm development phases. Environ. Sci. Technol. 55(17), 11948-11960.
927 Zhang, T., Xu, S., Yan, R., Wang, R., Gao, Y., Kong, M., Yi, Q. and Zhang, Y. 2022. Similar
928 geographic patterns but distinct assembly processes of abundant and rare bacterioplankton
929 communities in river networks of the Taihu Basin. Water Res. 211, 118057.
930 Zhang, W., Wang, Z., Zhao, Z., Wang, P., Wang, S., Ma, J. and Cheng, W. 2025. High-stable bimetallic
931 AgCu nanoalloys with core-shell structures for sustainable antibacterial and biofouling
932 mitigation in nanofiltration. Water Res. 271, 122986.
933 Zhang, Z., Cao, R., Jin, L., Zhu, W., Ji, Y., Xu, X. and Zhu, L. 2019. The regulation of
934 N-acyl-homoserine lactones (AHLs)-based quorum sensing on EPS secretion via ATP synthetic
935 for the stability of aerobic granular sludge. Sci. Total Environ. 673, 83-91.
936 Zhou, C.S., Wu, J.W., Liu, B.F., Ma, W.L., Yang, S.S. and Cao, G.L. 2022. (Micro) nanoplastics
937 promote the risk of antibiotic resistance gene propagation in biological phosphorus removal
938 system. J. Hazard. Mater. 431, 8.

939